Contents lists available at ScienceDirect

Materials Science & Engineering A

Effects of transformation-induced plasticity (TRIP) on tensile property improvement of $Fe_{45}Co_{30}Cr_{10}V_{10}Ni_{5-x}Mn_x$ high-entropy alloys

Junha Yang [a], Yong Hee Jo [a], Dae Woong Kim [a], Won-Mi Choi [a], Hyoung Seop Kim [a], Byeong-Joo Lee [a], Seok Su Sohn [b,*], Sunghak Lee [a,**]

[a] Center for High Entropy Alloys, Pohang University of Science and Technology, Pohang, 37673, Republic of Korea
[b] Department of Materials Science and Engineering, Korea University, Seoul, 02841, Republic of Korea

ARTICLE INFO

ABSTRACT

A new metastable high-entropy alloy (HEA) system was suggested by thermodynamic calculations based on the Gibbs free energies of FCC and HCP and the associated stacking fault energy (SFE). The $Fe_{45}Co_{30}Cr_{10}V_{10}Ni_{5-x}Mn_x$ (x = 0, 2.5, and 5 at.%) alloys were fabricated, and their tensile properties were evaluated at room and cryogenic temperatures. The relationship between the deformation mechanism and strain hardening behavior was investigated to reveal the role of deformation-induced martensitic transformation on tensile properties. The difference in Gibbs energy decreases with increasing Mn content, leading to the decreased SFE in sequence. At room temperature, ~60% of BCC martensite in the 5Mn HEA contributes effectively to the steady strain hardening, suppressing the plastic instability. This TRIP effect achieves much eminence in the cryogenic deformation, enabling the tensile strength to reach over 1.6 GPa due to 100% of BCC and HCP martensite. In addition to the fraction of martensite, the increased Mn content reduces a critical strain required to trigger the martensitic transformation and then raises the transformation rate. The present findings may provide a guide for the design of metastable HEAs to enhance tensile properties for cryogenic applications through adjusting SFE and TRIP effect.

1. Introduction

The twinning-induced plasticity (TWIP) has been well known as a dominating mechanism of face-centered-cubic (FCC) high- and medium-entropy alloys (HEAs and MEAs), leading to excellent mechanical properties at cryogenic temperature [1–4]. Recently, the transformation-induced plasticity (TRIP) mechanism, widely exploited in austenitic stainless and high-Mn steels, has also been introduced to the HEAs or MEAs to improve their properties further [5–9]. This metastable engineering and the associated novel alloy design strategies, thus, have engaged much attentions to enhance mechanical properties by adjusting the powerful deformation mechanisms.

Wang et al. [10] reported the mechanism of extraordinary strain hardening in an $Fe_{49.5}Mn_{30}Co_{10}Cr_{10}C_{0.5}$ (at.%) interstitial HEA under cryogenic conditions. The martensitic transformation from FCC to hexagonal close-packed (HCP) is enhanced, while the TWIP effect is prohibited, resulting in the tensile strength of 1.3 GPa and the ductility of 45% at 77 K. In contrast, Bae et al. [9] showed the martensitic transformation from FCC to body-centered-cubic (BCC) in an Fe_x (CoNi)$_{90-x}$Cr$_{10}$ MEA system, specifically in x = 60 at.% of Fe, which improved the tensile strength and ductility at cryogenic temperature to 1.5 GPa and 87%, respectively. The underlying mechanism of the $Fe_{60}Co_{15}Ni_{15}Cr_{10}$ alloy is associated with dislocation slip and deformation-induced martensitic transformation. Recently, Jo et al. [5] reported the metastable $V_{10}Cr_{10}Fe_{45}Co_xNi_{35-x}$ alloys (x = 10, 20, 30, and 35 at.%) triggering the FCC to BCC transformation during the cryogenic deformation. However, the BCC transformation stems from the intersections of HCP martensite lamellae, implying whose mechanism is different from that of the $Fe_{60}Co_{15}Ni_{15}Cr_{10}$ alloy. Although the discrepancy of the mechanisms is present between two FCC-BCC transformation systems, a common design strategy is based on the consideration of phase stability.

The TRIP mechanism under cryogenic conditions is also observed in metastable FCC alloys, such as stainless steels, high-Mn steels, and

* Corresponding author.
** Corresponding author.
E-mail addresses: sssohn@korea.ac.kr (S.S. Sohn), shlee@postech.ac.kr (S. Lee).

Fe–Co alloys [11–20]. The martensitic transformation behavior is known to depend on a stacking fault energy (SFE), and generally activates more at low SFE levels [21–24]. For HEAs or MEAs generating the BCC martensite at cryogenic temperature, however, the SFE has not been considered in designing new alloys yet. In other words, the studies concerning which elements or how much they affect the SFE and consequent transformation mechanism are still unclear. In this study, therefore, we designed $Fe_{45}Co_{30}Cr_{10}V_{10}Ni_{5-x}Mn_x$ (x = 0, 2.5, and 5 at.%) HEAs to investigate the role of Ni and Mn on the SFE and associated transformation mechanism. The SFE at 298 K was estimated based on the difference in Gibbs free energy between HCP and FCC at room temperature. The SFE at 0 K was also interpreted by using a molecular dynamics (MD) simulation with a second nearest-neighbor modified embedded-atom method (2NN MEAM) potential formalism [25]. Then, the TRIP mechanisms were analyzed in detail by correlating the SFE with microstructural evolutions during deformation. Based on this understanding, our primary objectives are to reduce the SFE from the reference HEA, to generate the martensitic transformation more, and accordingly to enhance cryogenic tensile properties of HEAs.

2. Experimental

2.1. Material fabrication

The $Fe_{45}Co_{30}Cr_{10}V_{10}Ni_{5-x}Mn_x$ (x = 0, 2.5, and 5 at.%) HEAs were fabricated by a vacuum induction melting route under an argon atmosphere using a melting equipment (MC100V, Indutherm, Germany). For convenience, the alloys are referred to as '0Mn', '2.5Mn', and '5Mn' according to the Mn content. Commercial pure-element powders were alloyed in a zirconia crucible to produce master alloys (weight; 150 g). The alloys were cast inside a graphite module (size; 100 × 35 × 8 mm). The chemical compositions were confirmed by the wet-chemical analysis by ICP-OES (Inductively Coupled Plasma-Optical Emission Spectroscopy) method, as listed in Table 1. The cast ingots were homogenized at 1373 K for 6 h, cleaned in a solution of 20%-HCl, sandblasted, and then cold-rolled with a reduction ratio of 75% to produce 1.5-mm-thick sheets. These sheets were annealed at 1273 K for 10–20 min in evacuated quartz ampules and water-quenched. The annealing times were adjusted with 10–20 min to make FCC grain size as identical as possible, which could examine the effects of the composition on FCC stability without considering the grain-size effect.

2.2. Microstructure characterization

Phases were identified by an X-ray diffraction (XRD, Cu K_α, scan rate; 2 deg min^{-1}), and volume fractions were measured by an XRD method studied by Moser et al. [26] using integrated intensities of $(110)_\alpha$, $(200)_\alpha$, $(211)_\alpha$, and $(220)_\alpha$ peaks for α'-martensite, $(10–10)_\varepsilon$, $(10–11)$ $(10–12)_\varepsilon$, and $(10–13)_\varepsilon$ peaks for ε-martensite, and $(111)_\gamma$, $(200)_\gamma$, $(220)_\gamma$, $(311)_\gamma$, and $(222)_\gamma$ peaks for austenite. Here, the present BCC, HCP, and FCC are equivalent to the α'-martensite, ε-martensite, and austenite, respectively. Phase characterization and analysis of the deformation behavior were performed using an electron back-scatter diffraction (EBSD, step size; 0.07 μm). EBSD specimens were polished mechanically and then electro-polished in a 92% acetic acid and 8% perchloric acid solution at 40 V in order to remove surface damages.

2.3. Mechanical property tests

Plate-type dog-bone specimens (gage length; 6.4 mm, width; 2.5 mm, thickness; 1 mm) were prepared with the tension direction parallel to the rolling direction. They were tensioned at a crosshead speed of 6.4 × 10^{-3} mm s^{-1} at room and cryogenic temperatures using a conventional testing machine (8801, Instron, USA, capacity; 100 kN). For the cryogenic test, a chamber was attached into the machine. Engineering stress-strain curves were calculated from the load-displacement data, and the elongation of gauge length was measured and calibrated after obtaining the load-displacement data from the test. All tests were performed three times for each datum.

2.4. Stacking fault energy calculation

Stacking fault energy (SFE) for the CoCrFeMnNiV senary system was calculated by using an atomistic simulation with a second nearest-neighbor modified embedded-atom method (2NN MEAM) potential formalism [25]. The interatomic potential parameters for the CoCrFeMnNi quinary system were already developed [27], and the expended potential parameters toward the CoCrFeMnNiV senary system will be reported separately. To compute SFEs, we performed a molecular dynamics (MD) simulation at 0 K. The perfect FCC crystal structure (perfect model) was prepared by depositing (111) atomic layers along the y-axis, and the top layer in the perfect crystal was deleted for the stacking fault model (SF model). The sample size was 154 × 76 × 156 Å, with 151200 atoms for the perfect model, and 154 × 73 × 156 Å, with 147000 atoms for the SF model. Periodic boundary conditions were applied to all directions, and the area of stacking fault was fixed for the SF model.

3. Results

3.1. HEA microstructures

The reference composition ($Fe_{45}Co_{30}Cr_{10}V_{10}Ni_5$, 0Mn HEA) was introduced in our previous study [5]. The 0Mn HEA shows a dislocation glide at room temperature and partly a small amount of BCC martensite along the deformation twin. At cryogenic temperature, a large amount of FCC to BCC martensitic transformation via intermediate HCP martensite occurs as the temperature decreases [5,28]. This TRIP mechanism frequently occurs in conventional austenitic steels or Fe–Co alloys [11–20]. As described in the Introduction part, the deformation-induced martensitic transformation depends on the SFE and activates more in low SFE regime [21–24]. Our major interest in this study, therefore, is to reduce the SFE from that of the reference 0Mn HEA, to evolve the martensitic transformation more, and consequently to improve tensile properties of HEAs. The SFE (Γ) is the Gibbs energy required to create an HCP platelet of only two atomic layers in thickness and is expressed by:

$$\Gamma = 2\rho \, \Delta G^{FCC \rightarrow HCP} + 2\sigma \qquad (1)$$

where ρ, $\Delta G^{FCC \rightarrow HCP}$, and σ are the molar surface density on {111} planes, molar Gibbs energy for FCC→HCP transformation, and FCC/HCP interfacial surface energy, respectively [29]. Based on the reference composition ($Fe_{45}Co_{30}Cr_{10}V_{10}Ni_5$, 0Mn HEA), Mn is added at the expense of Ni for controlling the SFE in metastable FCC alloys [5] in the present study. In other words, Ni and Mn contents are varied in the $Fe_{45}Co_{30}Cr_{10}V_{10}Ni_{5-x}Mn_x$ system. The difference in Gibbs free energy between HCP and FCC ($\Delta G^{FCC \rightarrow HCP}$, stability of HCP phase) was estimated using a CALPHAD approach with a Thermo-Calc software [30]. The TCFE2000 database and its upgraded version was used in this study [31–33]. This calculation considers the chemical contribution on the SFE alone; however, the SFE is also affected by the magnetic contribution. Curtze et al. [34] reported that the magnetic contribution on the SFE was negligible above Néel temperature of the FCC, indicating that

Table 1
Chemical compositions measured from the wet-chemical analysis by ICP-OES method for the $Fe_{45}Co_{30}Cr_{10}V_{10}Ni_{5-x}Mn_x$ HEAs. (unit: at.%).

HEA	Fe	Co	Cr	V	Ni	Mn
0Mn	45.55	30.07	9.92	9.68	4.78	0
2.5Mn	45.69	29.84	10.09	9.45	2.45	2.48
5Mn	45.65	29.85	10.04	9.55	0	4.91

the chemical contribution becomes dominant in the SFE. Thus, it is reasonable to access on the SFE using the free energy difference. In addition, the thermodynamic approach to calculate SFEs is not available below the room temperature. Instead, the SFE at 0 K for the CoCr-FeMnNiV senary system was calculated by using the molecular dynamics (MD) simulation.

Fig. 1(a) shows a variation of difference in Gibbs free energy between HCP and FCC ($\Delta G^{FCC \rightarrow HCP}$) due to the replacement of Ni by Mn at 298 K. The increase in Mn content leads to a decrease in $\Delta G^{FCC \rightarrow HCP}$, and it is expected to show an identical trend with the decrease in SFE (blue arrow mark in Fig. 1(a)). Fig. 1(b) shows the calculated SFE at 0 K from the atomistic simulation. The decrease in SFE corresponds to the decrease in $\Delta G^{FCC \rightarrow HCP}$ with increasing Mn content. The experimental verification of the microstructure and deformation mechanism for the designed alloys were investigated in detail as follows.

Fig. 2(a–c) shows EBSD phase and inverse pole figure (IPF) maps of the as-annealed 0Mn, 2.5Mn, and 5Mn HEAs. The average size of FCC grains (D_{FCC}) are shown below the maps. All HEAs consist of a single FCC-grain structure. The D_{FCC} is 9.7–9.8 μm in the three HEAs, which indicates that the initial microstructures of the as-annealed HEAs are almost similar.

Fig. 3(a–c) shows the XRD profiles of the three HEAs tensile-fractured at room and cryogenic temperatures as well as the as-annealed HEAs. The data of the as-annealed HEAs are identical to those of the EBSD (Fig. 2(a–c)), which shows a single FCC phase in the as-annealed HEAs. After the room-temperature tensile failure, the fraction of FCC (V_{FCC}) is 99.6% in the 0Mn HEA and decreases with increasing Mn content. In the 5Mn HEA, the V_{FCC} reaches 38%. The decreased amount of V_{FCC} corresponds to the increased fraction of BCC, indicating the martensitic transformation from FCC to BCC. The HCP is hardly observed for the specimen tensioned to a failure. After the tensile failure at cryogenic temperature, the V_{FCC} is 6.4% in the 0Mn HEA, unlike in the tensile failure at room temperature. The V_{FCC} decreases to 0% in the 5Mn HEA, where the martensitic transformation occurs most actively.

3.2. Room- and cryogenic-temperature tensile properties

Fig. 4(a and b) represents the engineering tensile stress-strain curves of the three HEAs. The tensile properties are listed in Table 2. Both tensile strength and ductility improve by 10 and 19% at room temperature, respectively, with increasing Mn content from 0 to 5 at.%. At cryogenic temperature, the 5Mn HEA shows the highest tensile strength of over 1.6 GPa, while the ductility decreases with increasing Mn content in contrast to the room-temperature deformation. As the Mn content increases, the tensile strength increases by 25%, while the ductility decreases by 20% compared to each for the 0Mn HEA. Regarding the flow behavior, the stress-strain curves at room temperature show a parabolic shape, while the curves tend to display a sigmoidal shape at cryogenic temperature [5,14,18,35]. Interestingly, the 5Mn HEA presents a typical sigmoidal curve, thereby leading to the twice higher tensile strength than the strength at room temperature. It is noted that this curve contains a plateau (a kind of easy deformation stage) at low strains.

Fig. 4(c and d) shows the strain-hardening rate of the HEAs. All the HEAs show a gradually decreasing rate at room temperature (Fig. 4(c)), although the rate remains from the true strain of 0.35 in the 5Mn HEA, as indicated by a green arrow. At cryogenic temperature, the curves of the three HEAs show a down-up-down mode (Fig. 4(d)). There exists a deep trough, *i.e.*, softening, in low true strains, which will be discussed later in the Discussion part. A critical strain required to raise the hardening rate decreases from 0.15 to 0.05 with increasing Mn content, while the overall strain-hardening rate increases. The peak hardening rate of the 5Mn HEA reaches ~7 GPa.

3.3. Room-temperature deformation mechanisms

The EBSD combined IQ-phase maps for the tensile specimen fractured at room temperature are shown in Fig. 5(a–c). The fractions of BCC and HCP (V_{BCC} and V_{HCP}) were measured and indicated beside each map. The deformation mechanism of the reference 0Mn HEA was studied in the previous study [5]. The primary mechanism is a dislocation glide with a very small amount of deformation twin. In addition, the HCP is not formed, but a tiny amount of BCC is formed in the 0Mn HEA (Figs. 3(a) and 5(a)). In order to provide more information on the room-temperature deformed structure, the EBSD combined IQ-IPF (Fig. S1, Supplementary material) maps are provided for the tensile specimen fractured at 298 K for the 0Mn, 2.5Mn, and 5Mn HEAs. Changes in the color contour inside grains indicate pronounced grain misorientations, indicating that the FCC accommodates such a large
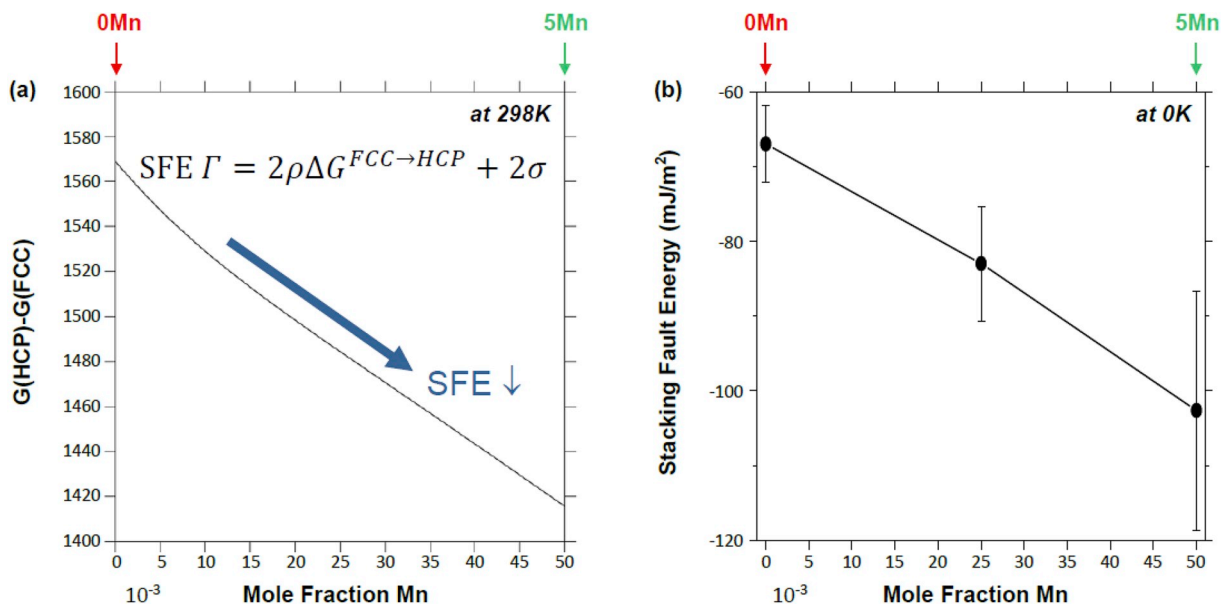

Fig. 1. (a) Difference in Gibbs free energy between HCP and FCC phases at 298 K ($\Delta G^{FCC \rightarrow HCP}$), which relates to the stacking fault energy (SFE) of the FCC phase. (b) SFE calculated from the atomistic simulation at 0 K. The decrease in $\Delta G^{FCC \rightarrow HCP}$ with increasing Mn content shows an identical trend with the decrease in SFE.
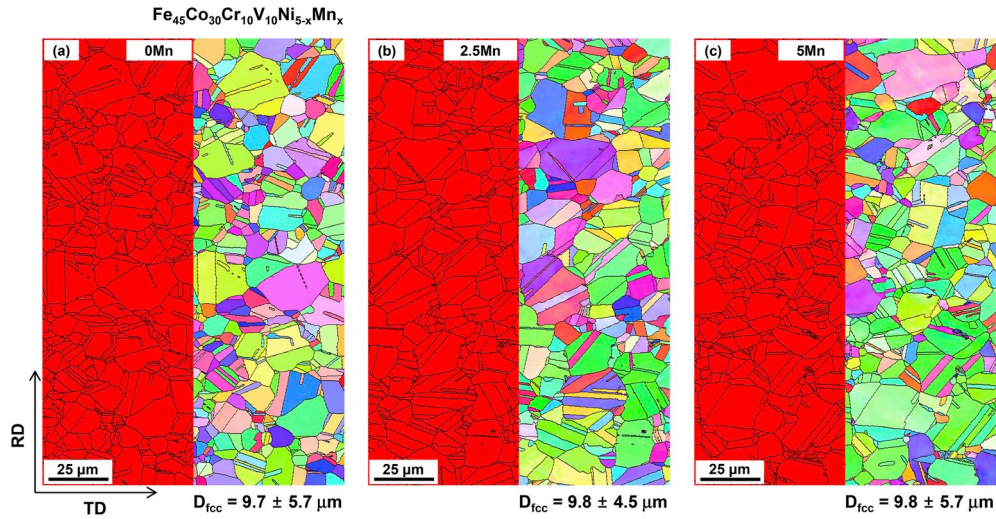
Fig. 2. Phase and inverse pole figure (IPF) maps from electron back-scatter diffraction (EBSD) analysis for the three as-annealed (a) 0Mn, (b) 2.5Mn, and (c) 5Mn HEAs. All HEAs show a single FCC phase of 9.7–9.8 μm in average grain size.
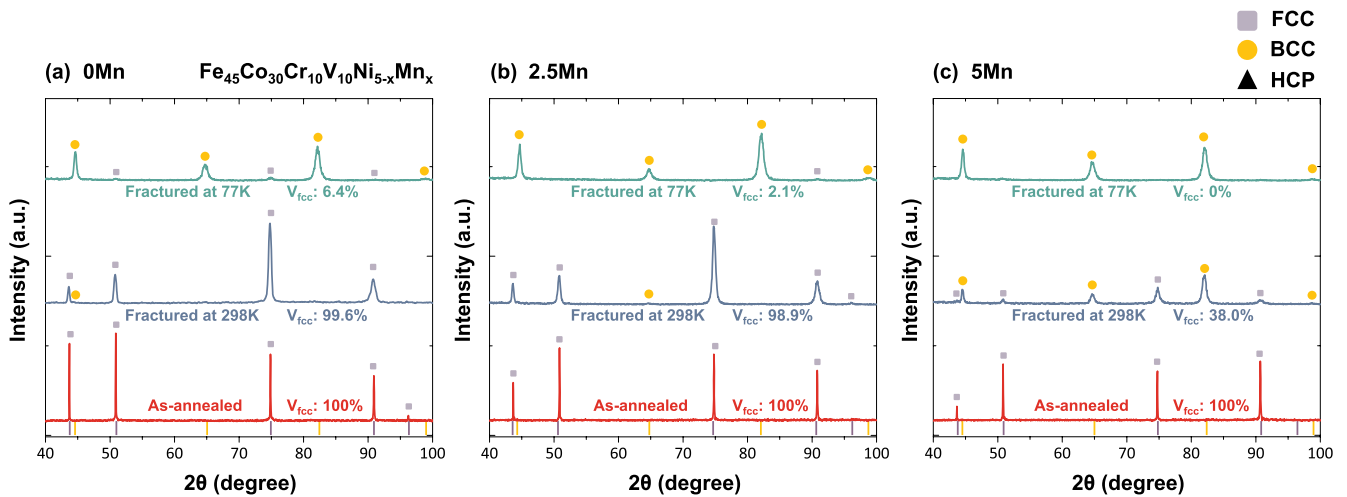

Fig. 3. X-ray diffraction profiles for the as-annealed state, tensile-fractured state at 298 K, and tensile-fractured state at 77 K of the (a) 0Mn, (b) 2.5Mn, and (c) 5Mn HEAs.

strain by dislocation glide [1,3].

A few BCC of 1.5 vol% generate after the tensile failure in the 2.5Mn HEA (Fig. 5(b)). It is interesting to note that the deformation twins are clearly visible for the 2.5Mn HEA, and the BCC martensite forms along these twins. This result implies that the twins are nucleation sites for the martensitic transformation [28]. The BCC accounts for 59% in the 5Mn HEA (Fig. 5(c)). In Fig. 5(c), nucleation sites of BCC martensite are hard to be identified because the EBSD map is obtained from the tensile fractured specimen. Thus, in order to reveal the room-temperature deformation mechanism of the 5Mn HEA, the interrupted tensile tests at room temperature and subsequent microstructural characterizations by EBSD and TEM were performed. Figs. S2(a–h) shows the IQ and phase maps at the true strains of 0.1, 0.2, 0.3, and 0.4 for the 5Mn HEA. In the IQ maps at the true strain of 0.2 or higher, sharp lines inside the FCC grains that were not detected in the phase map are observed and marked by white arrows. These lines are further analyzed by TEM, revealing that they are HCP martensite as shown in Figs. S3(b–d). Thus, the nucleation site for BCC martensite at room temperature changes from twins for the 0Mn and 2.5Mn HEAs to HCP for the 5Mn HEA. This is attributed to the reduction in SFE and the consequent stabilization of HCP (Fig. 1(a and b)) [28]. In all the HEAs, the measured V_{BCC} well corresponds to that of the XRD data of Fig. 3(a–c).

3.4. Cryogenic-temperature deformation mechanisms

According to the XRD data (Fig. 3(a–c)), the V_{BCC} at cryogenic temperature ranges 93–100% for the three HEAs, which hinders the detailed microstructural characterization. For the cryogenic deformation, thus, EBSD phase maps for the tensile specimen deformed to the true strain of 0.17 are shown in Fig. 5(d–f). The V_{BCC} is 14.7% in the 0Mn HEA and increases to 48.3% as the Mn content increases. The deformation twins are rarely observed in all the HEAs; instead, the HCP exists for the cryogenic deformation. It is noted that the BCC forms along the deformation twins for the 0Mn and 2.5Mn HEAs at room temperature; however, for the cryogenic deformation it forms along the HCP martensite. This result indicates the nucleation mechanism of BCC martensite varies from twins to HCP martensite with decreasing testing temperature. The temperature decrease results in the reduction in $\Delta G^{FCC \rightarrow HCP}$ and consequent SFE [28,29,34]. The deformation mechanism for the 0Mn and 2.5Mn HEAs changes from twins at room temperature to HCP martensite at cryogenic temperature, which is thus attributed to the stabilization of HCP [28].
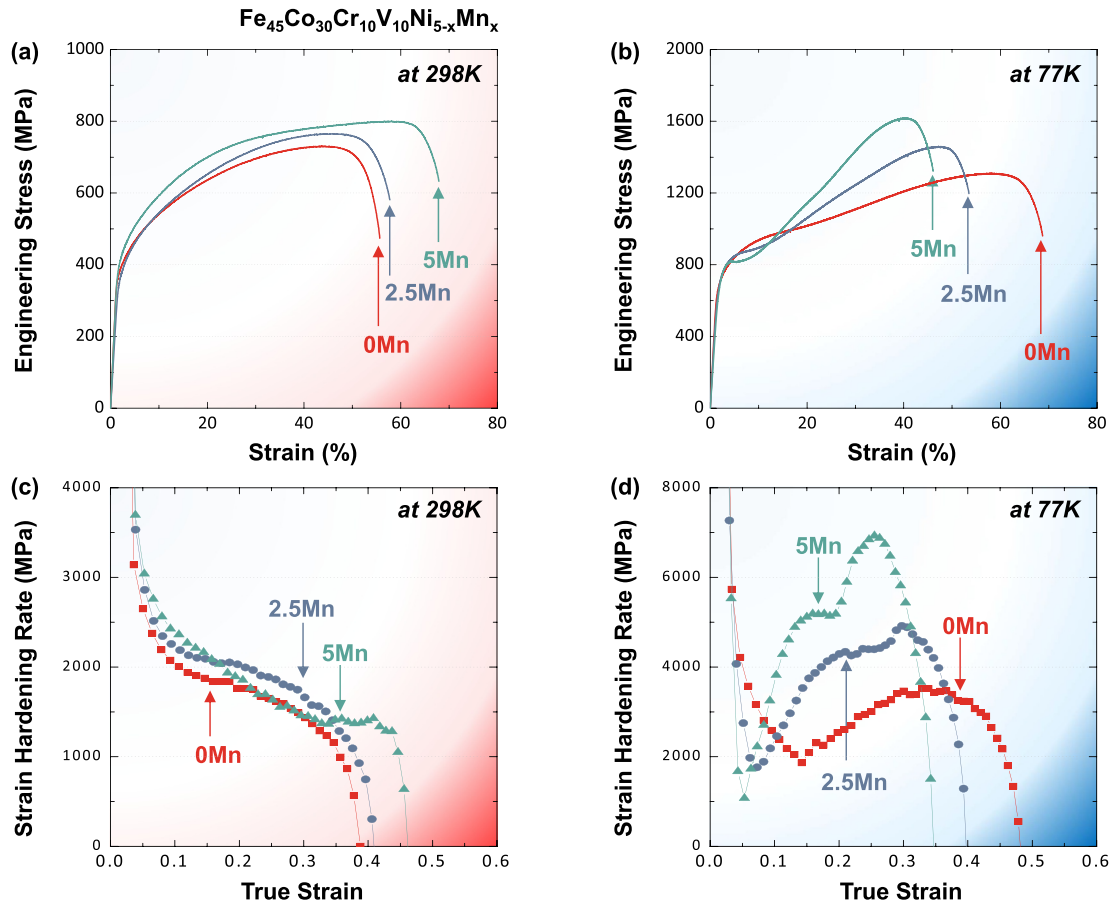
Fig. 4. Engineering stress-strain curves of the three HEAs tested at (a) 298 K and (b) 77 K. Strain hardening rate curves are obtained from the engineering stress-strain curves at (c) 298 K and (d) 77 K as a function of true strain.

Table 2
Room- and cryogenic-temperature tensile test results of the as-annealed 0Mn, 2.5Mn, and 5Mn HEAs.

Test Temperature	HEA	Yield Strength (MPa)	Tensile Strength (MPa)	Elongation (%)
298 K	0Mn	359 ± 4	732 ± 1	55.8 ± 0.9
	2.5Mn	345 ± 1	769 ± 4	57.2 ± 0.4
	5Mn	374 ± 2	802 ± 1	66.5 ± 1.3
77 K	0Mn	629 ± 6	1300 ± 8	67.0 ± 1.0
	2.5Mn	621 ± 8	1450 ± 15	53.9 ± 0.8
	5Mn	640 ± 7	1623 ± 10	46.8 ± 1.4

In order to more clearly reveal the BCC nucleation mechanism related to the HCP, EBSD analyses were conducted for the tensile specimen deformed to a true strain of 0.1 at cryogenic temperature. Fig. 6(a–c) shows EBSD phase, IPF, and image quality (IQ) maps for the specimen. The V_{BCC} and V_{HCP} are 30.7 and 3.4%, respectively, despite a small amount of deformation. It is clear that most of BCC show a bidirectional growth in Fig. 6(a and b). The HCP exists as a sharp line in the IQ map (Fig. 6(c)), and the BCC forms at its intersections having bright contrast and high IQ values. A specific region of interest is enlarged in Fig. 6(d and e), as indicated by a dotted box in the IPF map (Fig. 6(b)). The BCC and HCP have primary and secondary variants, which are indexed by α_1 and α_2, and ε_1 and ε_2, respectively. Each BCC or HCP developed in the same plane has the same orientation relationship (OR). The detailed OR of BCC or HCP is revealed by a pole figure analysis as shown in Fig. 6(f and g). The HCP nucleates from the FCC (γ), and has the Shoji-Nishiyama OR of $\{111\}_\gamma//\{0002\}_\varepsilon$ and $<110>_\gamma //<1120>_\varepsilon$. The BCC nucleates at the intersections of HCP, e.g., the α_1 forms along

the ε_1 with an intersection with the ε_2, and the BCC and HCP have Burgers OR of $\{110\}_\alpha //\{0002\}_\varepsilon$ and $<111>_\alpha//<1120>_\varepsilon$. The BCC and HCP, which grew in the same direction in Fig. 6(g), are found to be well associated with the OR. However, the HCP and BCC, which grew from different planes, relatively insufficiently satisfy the relations because they were not directly involved in each growth.

Based on the nucleation and growth behavior above, the total fraction of the martensitic transformation occurs 93.6% in the 0Mn alloy and increases to 100% with increasing Mn content (Fig. 3(a–c)). In order to investigate a strain dependency of the transformation, the interrupted tensile tests at 77 K were performed by true strains of 0.06, 0.1, 0.17, and 0.22. The measured V_{BCC} and V_{HCP} from the XRD analysis, which provides reliable data covering the wide area than the EBSD analysis, were plotted in Fig. 7(a–c) with standard deviations.

In all the HEAs, the V_{BCC} increases with increasing V_{HCP} in common. In the 0Mn HEA, the FCC phase transforms to the HCP and BCC phases from the strain of 0.1 (Fig. 7(a)). The V_{HCP} increases to 2.8% at 0.17, slightly decreases to 1.4% until 0.22, and then disappears at the failure. The V_{BCC} also increases to 12.1% from 0.17, and gradually rises to 93.6%. The volume fraction of total BCC and HCP martensite ($V_{BCC+HCP}$) is governed mainly by that of BCC due to the relatively low V_{HCP}. The 2.5Mn and 5Mn HEAs present a similar trend of increasing V_{BCC} and V_{HCP} (Fig. 7(b and c)), though overall transformation fractions are higher than those in the 0Mn HEA. Particularly in the 5Mn HEA, the total $V_{BCC+HCP}$ reaches 71.5% even at 0.22, indicating the highest strain dependency of martensitic transformation. The critical strain required for triggering the transformation is also associated with the dependency. The required strain in the 0Mn HEA is 0.17 at least, but decreases to 0.06 for the 2.5Mn and 5Mn HEAs. Considering that the initial V_{HCP} in the 2.5Mn HEA is only 0.5% at 0.06, it is more reasonable to discuss its peak
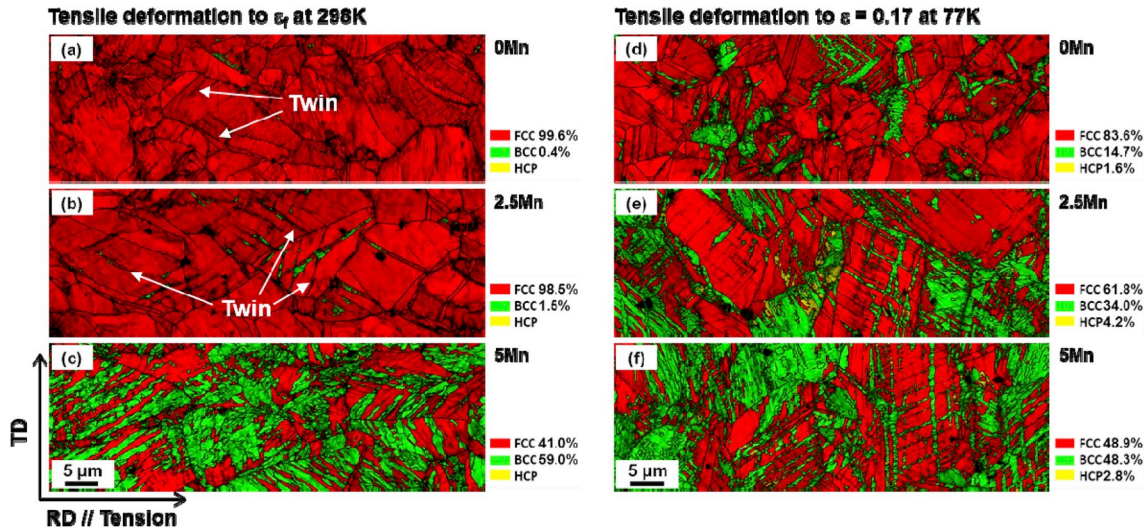
Fig. 5. EBSD combined IQ-phase maps of (a–c) the tensile specimen fractured at 298 K and (d–f) the tensile specimen deformed to the true strain of 0.17 at 77 K for the 0Mn, 2.5Mn, and 5Mn HEAs.
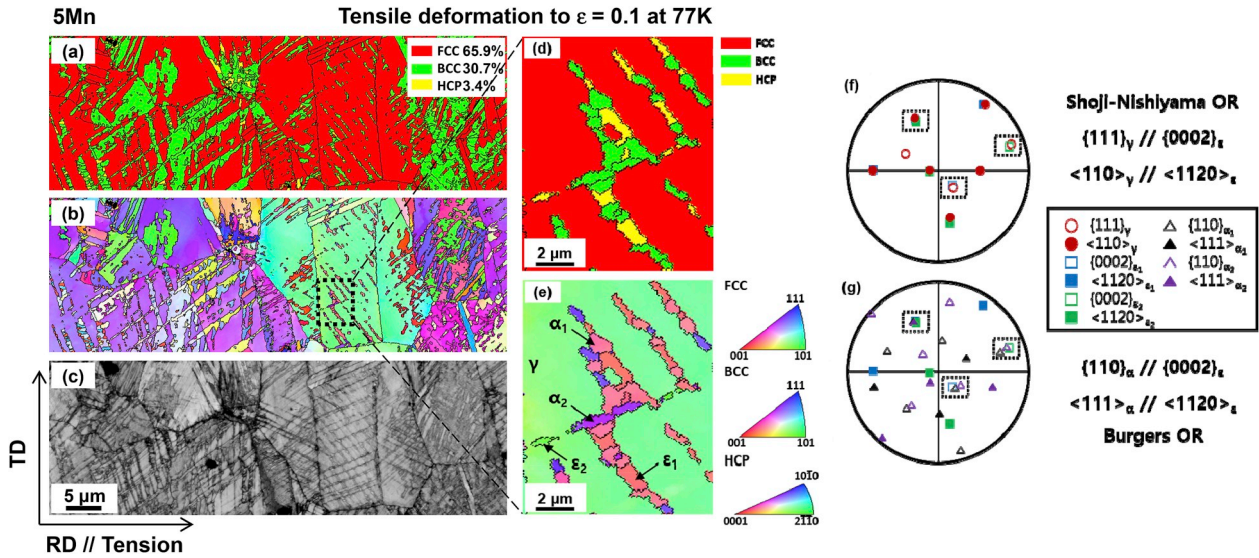

Fig. 6. EBSD (a) phase, (b) IPF, and (c) image quality (IQ) maps of the tensile specimen deformed to the true strain of 0.1 at 77 K. EBSD phase and IPF maps of an enlarged dotted-box area of Fig. 6(b) are shown in (d,e) to investigate orientation relationships between FCC, BCC, and HCP phases. Pole figures between (f) FCC and HCP phases and (g) BCC and HCP phases reveal the Shoji-Nishiyama relationship and Burgers relationship, respectively.
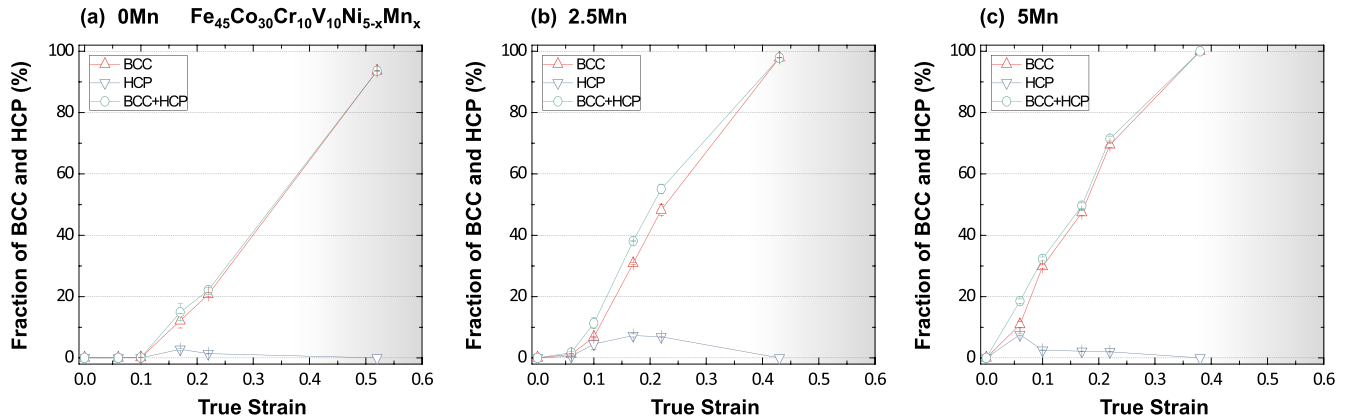

Fig. 7. Fractions of BCC and HCP phases (V_{BCC} and V_{HCP}) measured from the XRD analysis as a function of true strain for the tensile specimen deformed at 77 K of the (a) 0Mn, (b) 2.5Mn, and (c) 5Mn HEAs.

fraction. The peak V_{HCP} is 7.3% at 0.17 for the 2.5Mn HEA, while it is 7.6% at 0.06 for the 5Mn HEA. Therefore, the overall fraction and transformation rate of martensite increases as the Mn content increases in the $Fe_{45}Co_{30}Cr_{10}V_{10}Ni_{5-x}Mn_x$ HEA system.

4. Discussion

In this study, a new $Fe_{45}Co_{30}Cr_{10}V_{10}Ni_{5-x}Mn_x$ HEA system was presented with an aim to exploit the deformation-induced FCC to BCC martensitic transformation and its TRIP effect on strengthening. Since the SFE has not been much considered in the design of such alloys yet, the $\Delta G^{FCC \rightarrow HCP}$ and the SFE are calculated by using the CALPHAD approach and atomistic simulation, respectively. As the Mn content increases, the $\Delta G^{FCC \rightarrow HCP}$ decreased from 1570 to 1417 J/mol, and the SFE decreased from -67 to -102 mJ/m^2 (Fig. 1(a and b)). This approach and consequent decreased SFE correspond well to the experimental results in actual.

According to the deformation mechanism at room temperature of the three HEAs, the following deformation mechanism occurs in the order of increasing Mn content: deformation twinning and HCP martensite. The amount of FCC to BCC martensitic transformation increases with increasing Mn content (0.4, 1.1, and 62% in 0Mn, 2.5Mn, and 5Mn HEAs, respectively, Fig. 3(a–c)). At cryogenic temperature, the twins are hardly observed. Instead, the HCP transformation arises from the decreased SFE by a temperature effect. In addition, the overall fraction of martensite is higher than that at room temperature. The following remarkable findings can be characterized as the Mn content increases for the cryogenic deformation: (1) the BCC martensite forms along the HCP martensite or at its intersections, instead of along twins in the room-temperature deformation; (2) the V_{BCC} and V_{HCP} increase; (3) the critical strain required to trigger the martensitic transformation diminishes; (4) the transformation rate rises. All the variations affect tensile properties and strain hardening behavior significantly, which is discussed herein in detail.

Firstly, we discuss the strengthening mechanism and the reasons for high plasticity at room temperature. From the reference alloy (0Mn HEA), the increase of the Mn content results in the reduction in the SFE. At room temperature, the 2.5Mn HEA shows the relatively higher tensile strength, ductility, and strain hardening rate, compared to the reference 0Mn HEA, which is attributed to the slightly increased fractions of twins and BCC originated from reduced SFE [36]. The strain hardening rate of both HEAs decreases gradually, but that of the 2.5Mn HEA is slightly higher by ~200 MPa. The formation of deformation-induced martensite is known to relieve an accumulated strain at the matrix and to generate an additional large amount of mobile dislocation at martensite/matrix interfaces [18]. In addition, the deformation twins lead to a dynamic Hall-Petch effect, which refines the grain size during deformation [37–40]. Thus, such additional deformation mechanisms enhance a strain hardening capability. In this respect, the fraction of BCC martensite is significantly increased in the 5Mn HEA (~60%), leading to the highly-sustained high strain hardening and consequently delaying the tensile instability. This mechanism is a primary factor in enhancing both strength and ductility at room temperature. This effect arises from the limited close-packed slip system in the BCC than that in the FCC as well as the generation of geometrically necessary dislocations (GNDs) at the interface due to volume difference between BCC and FCC [18, 41–43]. This TRIP effect, thus, results in much higher tensile strength and ductility.

For the cryogenic deformation, the yield strength almost doubles from 345–374 MPa to 621–640 MPa due to a difficulty in dislocation movement [13,14,44–46]. It is also noted that the scale of y-axis in Fig. 4 (b,d) is twice larger than that in Fig. 4(a,c). The difficult movement of dislocation could enhance the strain hardening and tensile strength as well. Also, the amount of FCC to BCC martensitic transformation increases with decreasing temperature. The above two effects are decisive factors of enhanced strain hardening at cryogenic temperature.

Considering that the hardening rate in Fig. 4(d) behaves quite differently from Fig. 4(c); thus, it is apparent that the improved martensitic transformation and consequent TRIP effect have a remarkable role in determining the flow behavior (Fig. 3).

It is mentioned that the addition of Mn results in the decreased SFE and the increased $V_{BCC+HCP}$ in sequence. For the cryogenic deformation, the SFE is further reduced due to the dependency of SFE on temperature. Thus, all the HEAs shows a considerable martensitic transformation, which is confirmed by the phase fraction data in Figs. 3 and 7. In addition, the effects of BCC martensite on strain hardening, related to the slip system and the GNDs mentioned above, become more severe at cryogenic temperature [13,14,18,41–46]. Although the 0Mn HEA consists of 0.04% $V_{BCC+HCP}$ after the tensile failure at room temperature, it consists of 93.6% $V_{BCC+HCP}$ after the tensile failure at cryogenic temperature, which enables the strain hardening rate to reach ~3 GPa (Figs. 3(a) and 4(d)). This is the primary cause of the higher tensile strength and hardening rate at cryogenic temperature than those at room temperature. The 5Mn HEA consists of 100% $V_{BCC+HCP}$ after the tensile failure at cryogenic temperature, thereby leading to the tensile strength over 1.6 GPa (Fig. 4(d)). However, it should be considered that the transformation rate also enhances with increasing Mn content. The strain hardening rate reaches ~7 GPa due to the increased transformation rate, but the effect of TRIP on the delay of necking exhausts rapidly as well. This influence implies that the instability criterion, *i.e.*, Considère condition, achieves early and lowers the tensile ductility at cryogenic temperature [47].

Another interesting effect of Mn on martensitic transformation is related to the strain required to trigger the transformation. The critical strains for the 0Mn and 2.5Mn HEAs are corresponding to ~0.17 and ~0.06, respectively, because the V_{HCP} is close to 0.5% which could be assumed as the initiation of transformation. Considering that the V_{HCP} at a strain of 0.06 is 7.6% in the 5Mn HEA, the critical strain would be lower than the strain at least. Therefore, the strain required for the transformation decreases with increasing Mn content and decreasing SFE. The reason why the strain is discussed here is because it is closely associated with the strain to reverse a trend of down-up-down behavior in the hardening rate curve (Fig. 4(d)). The strains at reversal are 0.15, 0.07, and 0.05, which are equivalent very well to the critical strain for martensitic transformation. This finding also demonstrates that the martensitic transformation has a crucial role in improving the strain hardening rate. As the Mn content increases, FCC to BCC transformation via intermediate HCP martensite occurs more rapidly (Fig. 7(a–c)). In other words, the SFE and $\Delta G^{FCC \rightarrow HCP}$ are reduced (Fig. 1(a and b)) to stabilize the HCP, further activating the FCC-HCP transformation. Then, the HCP-BCC transformation is also more activated as the Mn content increases. According to the SFE reduction, thus, the transformation rate rises, and the critical strain required to trigger the martensitic transformation diminishes. In summary, the correlation between SFE and FCC-BCC transformation can be related to the fact that the decrease in SFE affects the acceleration of nucleation and the growth of BCC martensite in the present alloys whose potential BCC fractions are not much different according to the Mn content.

The FCC-BCC martensitic transformation mechanism of the $Fe_{45}Co_{30}Cr_{10}V_{10}Ni_{5-x}Mn_x$ HEA is defined by a strain-induced martensitic transformation [5,15]. The strain-induced transformation occurs at new nucleation sites created by intersections of microscopic shear bands (stacking faults, deformation twin, and HCP martensite) during the plastic deformation [15]. It is noteworthy that the sigmoidal shape of flow behavior at cryogenic temperature appears in contrast to the parabolic shape for the room-temperature tension, although the mechanism was not clearly identified in this study. The sigmoidal behavior becomes severe with increasing Mn content, and there exists a small stress drop at the initial deformation for the 5Mn HEA, as shown in Fig. 4 (d). This drop is called a 'strain softening' phenomenon, mainly attributing to the decreased strain hardening rate at the initial deformation due to the FCC-HCP transformation, as treated in metastable Fe–Mn

alloys or stainless steels [5,15,18,47,48]. Thereafter, the BCC martensite is formed by consuming the HCP martensite, thereby enhancing the strain hardening rate. This tendency implies that the FCC-BCC martensitic transformation occurs via the intermediate HCP martensite at cryogenic temperature. According to Bhadeshia et al. [42], a large transformation shear by the FCC to HCP transformation offsets a contraction in atomic spacing originated from a difference of crystal structure. During the HCP formation, thus, almost no net change occurs in lattice volume between FCC and HCP in actual, resulting in the strain softening or yield plateau in the flow behavior at low strain levels. Our finding is well corresponding to this mechanism; in other words, the increase in Mn content leads to the increase in V_{HCP} and the severity of strain softening in sequence.

5. Conclusions

A metastable $Fe_{45}Co_{30}Cr_{10}V_{10}Ni_{5-x}Mn_x$ HEA system was suggested, based on the Gibbs free energies of FCC and HCP and the associated SFE. The 0Mn, 2.5Mn, and 5Mn HEAs were fabricated, and then their tensile properties were evaluated at room and cryogenic temperatures. The deformation-structure evolution was investigated by XRD and EBSD analyses in detail. The following conclusions are drawn by the correlation of deformation mechanisms with the strain hardening behavior.

(1) The Gibbs free energy difference between FCC and HCP ($\Delta G^{FCC \to HCP}$, stability of HCP phase) was considered to estimate the SFE using the CALPHAD approach. As the Mn content increases, the $\Delta G^{FCC \to HCP}$ decreased from 1570 to 1417 J/mol, and the SFE decreased from -67 to -102 mJ/m^2.

(2) The deformation mechanism at room temperature occurred in the order of the Mn content, which was characterized by dislocation glide, additional deformation twinning and martensitic transformation of ~1% of BCC, and martensitic transformation of ~60% of BCC. A plenty of BCC martensite in the 5Mn HEA contributed effectively to the steady strain hardening to suppress plastic instability.

(3) At cryogenic temperature, the twins were hardly observed; instead, the HCP transformation arose due to the decreased SFE by a temperature effect. In addition, the overall fraction of martensite was higher than that at room temperature. The deformation-induced BCC martensite beneficially contributed to the significant improvement of strain hardening and consequently both strength and ductility.

(4) The $V_{BCC+HCP}$ reached 100% in the 5Mn HEA after the tensile failure, thereby leading to the tensile strength over 1.6 GPa. Due to the enhanced transformation rate, however, the effect of TRIP on the delay of necking exhausted rapidly as well, and lowered the tensile ductility.

(5) The Mn addition and consequent decreased SFE reduced the critical strain required to trigger the martensitic transformation. The critical strains for the HEAs in the order of Mn content were ~0.17, ~0.06, and <0.06, respectively, which were corresponding closely to the strain to reverse a trend of down-up-down behavior in the hardening rate curve. This finding demonstrated that the martensitic transformation had a crucial role in enhancing the strain hardening rate.

Author contributions

Junha Yang: Methodology, Formal analysis, Investigation, Data Curation, Visualization, Yong Hee Jo: Conceptualization, Methodology, Validation, Visualization, Dae Woong Kim: Formal analysis, Investigation, Visualization, Won-Mi Choi: Software Programming, Formal analysis, Investigation, Hyoung Seop Kim: Resources, Project administration, Funding acquisition, Writing - Review & Editing, Supervision, Byeong-Joo Lee: Software Programming, Formal analysis, Writing - Review & Editing, Supervision, Seok Su Sohn: Conceptualization, Visualization, Funding acquisition, Writing - Review & Editing, Supervision, Sunghak Lee: Conceptualization, Project administration, Writing - Original Draft, Writing - Review & Editing, Supervision

Declaration of competing interests

The authors declare that they have no known competing financial interests or personal relationships that could have appeared to influence the work reported in this paper.

Acknowledgments

Appendix A. Supplementary data

Supplementary data to this article can be found online at https://doi.org/10.1016/j.msea.2019.138809.

References

[1] B. Gludovatz, A. Hohenwarter, K.V.S. Thurston, H. Bei, Z. Wu, E.P. George, R.O. Ritchie, Exceptional damage-tolerance of a medium-entropy alloy CrCoNi at cryogenic temperatures, Nat. Commun. 7 (2016), 10602.

[2] M.J. Jang, H. Kwak, Y.W. Lee, Y. Jeong, J. Choi, Y.H. Jo, W.-M. Choi, H.J. Sung, E.Y. Yoon, S. Praveen, S. Lee, B.-J. Lee, M.I. Aal, H.S. Kim, Plastic deformation behavior of 40Fe-25Ni-15Cr-10Co-10V high-entropy alloy for cryogenic applications, Met. Mater. Int. 25 (2019) 277–284.

[3] B. Gludovatz, A. Hohenwarter, D. Catoor, E.H. Chang, E.P. George, R.O. Ritchie, A fracture-resistant high-entropy alloy for cryogenic applications, Science 345 (2014) 1153–1158.

[4] Y.H. Jo, S. Jung, W.M. Choi, S.S. Sohn, H.S. Kim, B.-J. Lee, N.J. Kim, S. Lee, Cryogenic strength improvement by utilizing room-temperature deformation twinning in a partially recrystallized VCrMnFeCoNi high-entropy alloy, Nat. Commun. 8 (2017), 15719.

[5] Y.H. Jo, W.-M. Choi, D.G. Kim, A. Zargaran, S.S. Sohn, H.S. Kim, B.-J. Lee, N.J. Kim, S. Lee, FCC to BCC transformation-induced plasticity based on thermodynamic phase stability in novel $V_{10}Cr_{10}Fe_{45}Co_xNi_{35-x}$ medium-entropy alloys, Sci. Rep. 9 (2019), 2948.

[6] Z. Li, K.G. Pradeep, Y. Deng, D. Raabe, C.C. Tasan, Metastable high-entropy dual phase alloys overcome the strength–ductility trade-off, Nature 534 (2016) 227–230.

[7] D. Wei, X. Li, J. Jiang, W. Heng, Y. Koizumi, W.-M. Choi, B.-J. Lee, H.S. Kim, H. Kato, A. Chiba, Novel Co-rich high performance twinning-induced plasticity (TWIP) and transformation-induced plasticity (TRIP) high-entropy alloys, Scr. Mater. 165 (2019) 39–43.

[8] H. Huang, Y. Wu, J. He, H. Wang, X. Liu, K. An, W. Wu, Z. Lu, Phase-transformation ductilization of brittle high-entropy alloys via metastability engineering, Adv. Mater. 29 (2017), 1701678.

[9] J.W. Bae, J.B. Seol, J. Moon, S.S. Sohn, M.J. Jang, H.Y. Um, B.-J. Lee, H.S. Kim, Exceptional phase-transformation strengthening of ferrous medium-entropy alloys at cryogenic temperatures, Acta Mater. 161 (2018) 388–399.

[10] Z. Wang, W. Lu, D. Raabe, Z. Li, On the mechanism of extraordinary strain hardening in an interstitial high-entropy alloy under cryogenic conditions, J. Alloy. Comp. 781 (2019) 734–743.

[11] Y. Tomota, M. Strum, J.W. Morris, The relationship between toughness and microstructure in Fe-high Mn binary alloys, Metall. Trans. A 18A (1991) 1073–1081.

[12] J.W. Morris Jr., S.K. Hwang, K.A. Yushchenko, V.I. Belotzerkovetz, O.G. Kvasnevskii, Fe-Mn alloys for cryogenic use: a brief survey of current research, Adv. Cryog. Eng. 24 (1978) 91–102.

[13] S.S. Sohn, S. Hong, J. Lee, B.-C. Suh, S.-K. Kim, B.-J. Lee, N.J. Kim, S. Lee, Effects of Mn and Al contents on cryogenic-temperature tensile and Charpy impact properties in four austenitic high-Mn steels, Acta Mater. 100 (2015) 39–52.

[14] T.S. Byun, N. Hashimoto, K. Farrell, Temperature dependence of strain hardening and plastic instability behaviors in austenitic stainless steels, Acta Mater. 52 (2004) 3889–3899.

[15] G.B. Olson, M. Cohen, Kinetics of strain-induced martensitic nucleation, Metall. Trans. A 6A (1975) 791–795.

[16] Y. Tomota, M. Strum, J.W. Morris, Microstructual dependence of Fe-high Mn tensile behavior, Metall. Trans. A 17A (1986) 537–547.

[17] S. Kim, D. Jeong, H. Sung, Reviews on factors affecting fatigue behavior of high-Mn steels, Met. Mater. Int. 24 (2018) 1–14.

[18] A.K. De, J.G. Speer, D.K. Matlock, D.C. Murdock, M.C. Mataya, R.J. Comstock, Deformation-induced phase transformation and strain hardening in type 304 austenitic stainless steel, Metall. Mater. Trans. A 37A (2006) 1875–1886.

[19] Q. Gao, M. Gong, Y. Wang, F. Qu, J. Huang, Phase transformation and properties of Fe-Cr-Co alloys with low cobalt content, Mater. Trans. 56 (2015) 1491–1495.

[20] T. Nishizawa, K. Ishida, The Co-Fe (Cobalt-Iron) system, Bull. Alloy Phase Diagrams 5 (1984) 250–259.

[21] M. Ghasri-Khouzani, J.R. McDermid, Effect of carbon content on the mechanical properties and microstructural evolution of Fe-22Mn-C steels, Mater. Sci. Eng. A 621 (2015) 118–127.

[22] G. Frommeyer, U. Brüx, P. Neumann, Supra-ductile and high-strength manganese-TRIP/TWIP steels for high energy absorption purposes, ISIJ Int. 43 (2003) 438–446.

[23] Y.-K. Lee, C. Choi, Driving force for $\gamma \rightarrow \varepsilon$ martensitic transformation and stacking fault energy of γ in Fe–Mn binary system, Metall. Mater. Trans. A 31A (2000) 355–360.

[24] K. Sato, M. Ichinose, Y. Hirotsu, Y. Inoue, Effects of deformation induced phase transformation and twinning on the mechanical properties of austenitic Fe–Mn–Al alloys, ISIJ Int. 29 (1989) 868–877.

[25] B.-J. Lee, M.I. Baskes, Second nearest-neighbor modified embedded-atom-method potential, Phys. Rev. B. 62 (2000), 8564.

[26] N.H. Moser, T.S. Gross, Y.P. Korkolis, Martensite formation in conventional and isothermal tension of 304 austenitic stainless steel measured by x-ray diffraction, Metall. Mater. Trans. A 45A (2014) 4891–4896.

[27] W.-M. Choi, Y.H. Jo, S.S. Sohn, S. Lee, B.-J. Lee, Understanding the physical metallurgy of the CoCrFeMnNi high-entropy alloy: an atomistic simulation study, Npj Comput. Mater. 4 (2018) 1.

[28] Y.H. Jo, D.G. Kim, M.C. Jo, K.-Y. Doh, S.S. Sohn, D. Lee, H.S. Kim, B.-J. Lee, S. Lee, Effects of deformation-induced BCC martensitic transformation and twinning on impact toughness and dynamic tensile response in metastable VCrFeCoNi high-entropy alloy, J. Alloy. Comp. 785 (2019) 1056–1067.

[29] S. Allain, J.-P. Chateau, O. Bouaziz, S. Migot, N. Guelton, Correlations between the calculated stacking fault energy and the plasticity mechanisms in Fe-Mn-C alloys, Mater. Sci. Eng. A 387–389 (2004) 158–162.

[30] B. Sundman, B. Jansson, J.-O. Andersson, The thermo-calc databank system, Calphad 9 (1985) 153–190.

[31] B.-J. Lee, B. Sundman, Thermo-calc. Database TCFE2000, Upgraded by, KTH, Stockholm, 1999.

[32] K.-G. Chin, H.-J. Lee, J.-H. Kwak, J.-Y. Kang, B.-J. Lee, Thermodynamic calculation on the stability of $(Fe,Mn)_3AlC$ carbide in high aluminum steels, J. Alloy. Comp. 505 (2010) 217–223.

[33] W.-M. Choi, S. Jung, Y.H. Jo, S. Lee, B.-J. Lee, Design of new face-centered cubic high entropy alloys by thermodynamic calculation, Met. Mater. Int. 23 (2017) 839–847.

[34] S. Curtez, V.-T. Kuokkala, Dependence of tensile deformation behavior of TWIP steels on stacking fault energy, temperature and strain rate, Acta Mater. 58 (2010) 5129–5141.

[35] M. Onyuna, H. Oettel, U. Martin, A. Weiss, On the deformation behavior and martensitic transformations of metastable austenitic steels, Adv. Eng. Mater. 6 (2004) 529–535.

[36] T.-H. Lee, E. Shin, C.-S. Oh, H.-Y. Ha, S.-J. Kim, Correlation between stacking fault energy and deformation microstructure in high-interstitial-alloyed austenitic steels, Acta Mater. 58 (2010) 3173–3186.

[37] S. Asgari, E. El-Danaf, S.R. Kalidindi, R.D. Doherty, Strain hardening regimes and microstructural evolution during large strain compression of low stacking fault energy fcc alloys that form deformation twins, Metall. Mater. Trans. A 28A (1997) 1781–1795.

[38] J.-K. Hwang, Deformation behaviors of flat rolled wire in twinning-induced plasticity steel, Met. Mater. Int. (2019) 1–14.

[39] N.H. Heo, Y.-U. Heo, S.K. Kwon, N.J. Kim, S.-J. Kim, H.-C. Lee, Extended Hall-Petch relationships for yield, cleavage and intergranular fracture strengths of bcc steel and its deformation and fracture behaviors, Met. Mater. Int. 24 (2018) 265–281.

[40] O. Bouaziz, S. Allain, C.P. Scott, P. Cugy, D. Barbier, High manganese austenitic twinning induced plasticity steels: a review of the microstructure properties relationships, Curr. Opin. Solid State Mater. Sci. 15 (2011) 141–168.

[41] I. Tamura, T. Maki, H. Hato, Morphology of strain-induced martensite and the transformation-induced plasticity in Fe-Ni and Fe-Cr-Ni alloys, Trans. ISIJ 10 (1970) 163–172.

[42] H.K.D.H. Bhadeshia, Worked Examples in the Geometry of Crystals, The Institute of Metals, 2006.

[43] B.B. He, W. Xu, M.X. Huang, Increase of martensite start temperature after small deformation of austenite, Mater. Sci. Eng. A 609 (2014) 141–146.

[44] G.E. Dieter, D. Bacon, Mechanical Metallurgy, McGraw-Hill, London, 1986.

[45] M.A. Meyers, K.K. Chawla, Mechanical Behavior of Materials, Prentice-Hall, 1999.

[46] R.W. Hertzberg, Deformation and Fracture Mechanics of Engineering Materials, John Wiley & Sons, 1989.

[47] G.L. Huang, D.K. Matlock, G. Krauss, Martensite formation, strain rate sensitivity, and deformation behavior of type 304 stainless steel sheet, Metall. Trans. A 20 (1989) 1239–1246.

[48] K. Datta, R. Delhez, P.M. Bronsveld, J. Beyer, H.J.M. Geijselaers, J. Post, A low-temperature study to examine the role of ε-martensite during strain-induced transformations in metastable austenitic stainless steels, Acta Mater. 57 (2009) 3321–3326.